Optical and theoretical study of $NaCrP_2O_7$: A look through Neuhauser model and Racah theory

H. Souissi[1]*, S. Kammoun[1], E. Dhahri[1], E. López-Lago[2]

[1]*Applied Physics Laboratory, Faculty of Sciences, Sfax University, BP 1171, 3000, Sfax, Tunisia*

[2] *Departamento de Física Aplicada, Facultade de Óptica e Optometría, Campus Vida, Universidade de Santiago de Compostela (USC), 15782 Galicia, Spain.*

*Corresponding author: souissi.hajer.fss@gmail.com

Abstract

The $NaCr(P_2O_7)$ sample was synthesized using the solid-state reaction method. X-ray diffractogram and Rietveld refinement confirmed the formation of a monoclinic structure with the $P2_1/a$ space group. The morphology and homogeneity of the chemical composition were identified through Scanning Electron Microscopy (SEM) and Energy Dispersive X-ray analysis (EDX). The optical absorption spectrum was measured in the wavelength range of 200 nm to 833 nm at room temperature. The direct optical band gap of the $NaCr(P_2O_7)$ material was estimated to be 2.9 eV. The Urbach energy of the $NaCr(P_2O_7)$ material was determined to be 0.44 eV. The absorption spectrum of $NaCr(P_2O_7)$ sample shows the presence of interference dip on the lowest energy band $^4T_{2g}(^4F)$. This interference results from the interaction via spin-orbit coupling between states $^2E_g(^2G)$ and $^4T_{2g}(^4F)$ with different multiplicities of spins. We have analyzed this phenomenon through the Neuhauser model based on coupled potential energy surfaces. From the Neuhauser results, the electronic structure of Cr^{3+} ($3d^3$) ions in $NaCr(P_2O_7)$ sample was determined. Thus, a reliable calculation of Racah and crystal-field parameters has been obtained, leading to a good agreement between both experimental and theoretical energy levels. We employed the coupled potential energy surface model to study the coupling between states that have different multiplicities of spin and demonstrate the impact of spin-orbit interactions.

Keywords: $NaCr(P_2O_7)$ material; Neuhauser model, crystal structure; Optical band-gap; crystal field theory.

1. Introduction

Recently, many investigations on transition metal phosphates have been performed. These compounds, which contain MO_6 octahedra and PO_4 tetrahedra, demonstrate a variety of structural compositions. One of specific area of interest are sodium diphosphate ceramics with the chemical formula $NaM(P_2O_7)$, where M represents transition metals (Cr, Al, Fe, Y, Co …) [1-3]. Among these materials, $NaCr(P_2O_7)$ has many uses as ceramic, ferroelectric, electric, solid electrolyte, catalyst, and nonlinear optical material [4-7]. Despite extensive research across various domains, there has been limited exploration specifically focused on the optical properties of $NaCrP_2O_7$. Despite extensive research across various domains, there has been limited exploration specifically focused on the optical properties of $NaCrP_2O_7$. This material could be interesting owing to the presence of the metallic element Chromium (Cr) which can enhance its optical properties [8,9]. The chromium exhibits an octahedral environment and is present in smaller amounts than phosphorus.

The objective of this article is to explore various aspects. Initially, our focus will be on the preparation and on the structural examination of the $NaCrP_2O_7$ compound. Subsequently, we aim to present significant optical parameters: the band gap energy (E_g) and Urbach energy (E_u). In addition, we employ the Neuhauser model to study the feature seen in the absorption band of Cr^{3+} ions. This study is performed to demonstrate the origin of interference dips that appear in the absorption spectrum. Lastly, an investigation based on crystal field theory, employing Racah tensor algebraic methods, was carried out for the $Cr^{3+}(3d^3)$ within an O_h site symmetry. It is noteworthy that a limited number of studies have employed crystal field theory for a thorough and systematic examination of the absorption spectra of the mentioned compound.

2. Experimental details

To produce $NaCrP_2O_7$ compound a solid-state procedure was used at high temperatures. In a mortar, the components (Na_2CO_3, Cr_2O_3, and NH_2- H_4PO_4) were mixed and ground in conformity with the chemical transformation:

$$Na_2CO_3 + Cr_2O_3 + (4\ NH_4H_2PO_4) \rightarrow 2NaCrP_2O_7 + 4NH_3 + 6H_2O + CO_2 \quad (\mathbf{1})$$

In the first time, they were heated slowly at 573 K for 9 h to eliminate NH_3, H_2O, and CO_2, and their stoichiometric quantities were measured. After being calcined, the powder was transformed into cylindrical pieces and heated for 11 hours at 973 K. To evaluate phase purity, XRD patterns were obtained and refined with the assistance of a Phillips powder diffractometer PW 1710. The measurements encompassed a broad spectrum of Bragg angles from 10° to 100°, employing copper CuKα radiation (λ = 1.5405 Å). In addition, samples were analyzed using a Zeiss EVO LS15

Scanning Electron Microscope (SEM) coupled with Energy Dispersive X-ray Spectroscopy (EDX) for detailed imaging and elemental analysis. The absorbance and reflectance spectra were obtained by utilizing a Perkin Elmer Lambda 1050 spectrophotometer at ambient temperature, covering the wavelength range from 200 to 833 nm.

3. Results and discussion

3.1. Structural and morphological studies

The crystal structure of the $NaCrP_2O_7$ was analyzed based on powder X-ray diffraction (XRD) data. The results of (XRD) pattern of our sample taken at room temperature in the 2θ range (10-100) with a step width of 0.02 is shown in Figure 1. The XRD refinement were also performed by Rietveld refinement using Fullprof software [10]. All the reflection peaks are indexed in the monoclinic system with $P2_1/a$ space group. Peaks corresponding to $NaCrP_2O_7$ are indicated, confirming the presence of the desired phase. The unit cell dimensions are a = 13.031(2) Å, b = 22.539(5) Å, c = 5.927(5)Å, and β =91.633(7)°. The reliability factors R_{wp} and R_p was found at 6.4 and 7.3 respectively. The goodness-of-fit (chi-square factor χ) is 3.6, this result shows a good quality of fit.

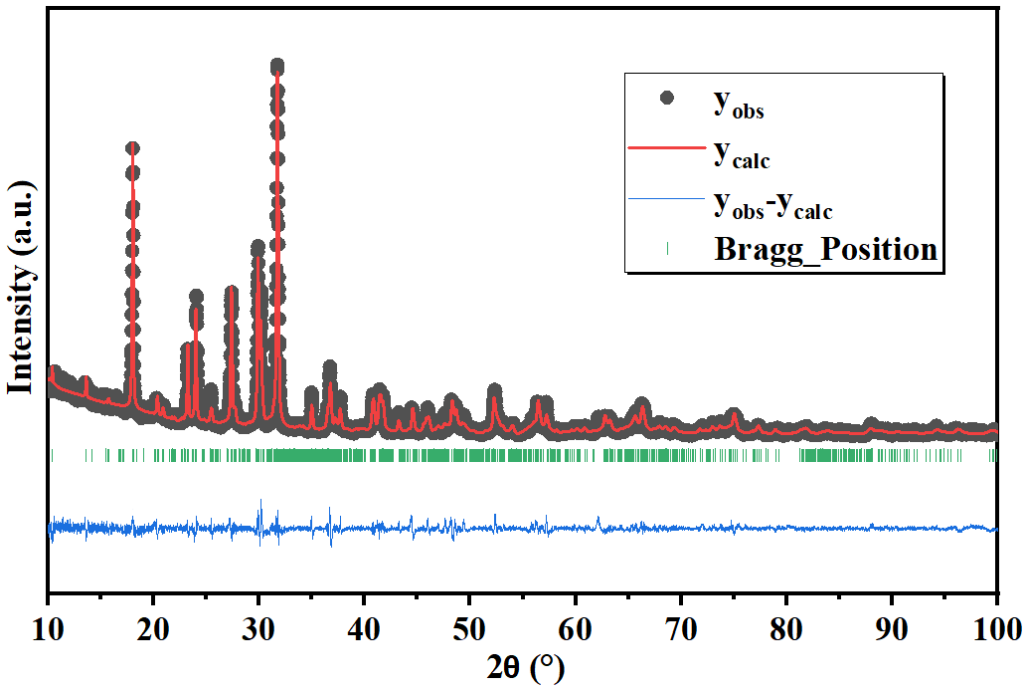

Figure 1. The X-Ray Diffraction (XRD) pattern of the synthesized sample (black) and Rietveld refinement for the $NaCrP_2O_7$ sample overlaid with the standard reference pattern for the $NaCrP_2O_7$ phase (red, JCPDS no. 96-154-1856).

The structure of this compound is shown in Figure 2. In this structure, the Cr^{3+} site is octahedral coordination (O_h point group) and it is surrounded by O ligands.

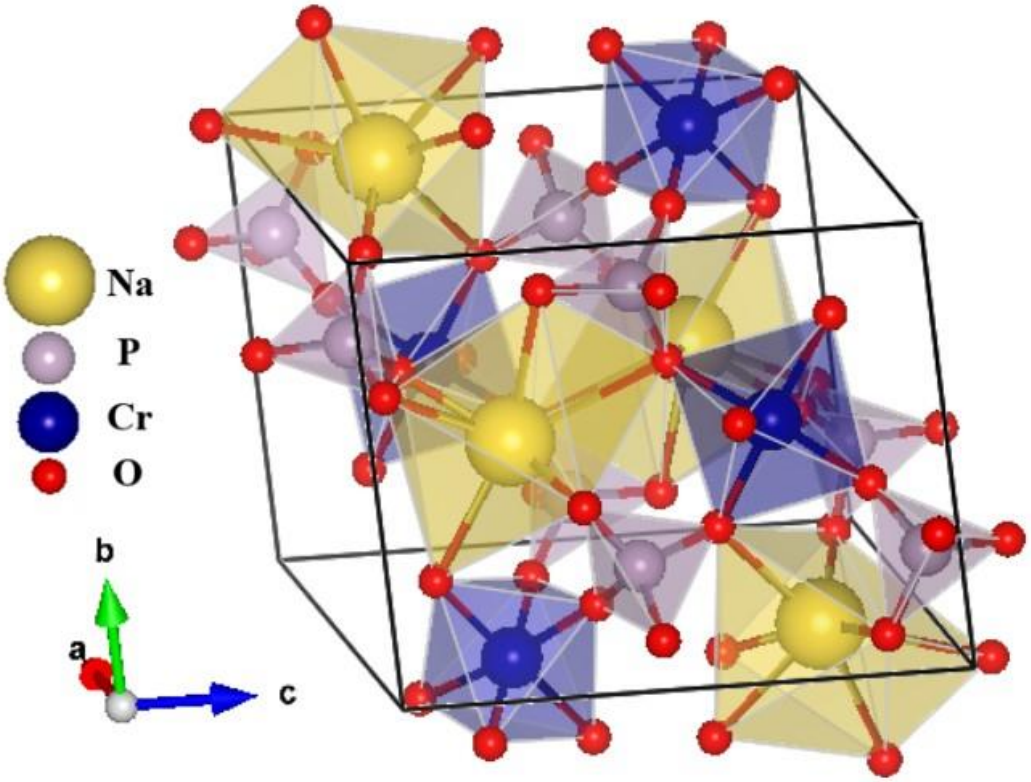

Figure 2. Unit cell of $NaCrP_2O_7$ as drawn with the Vesta software [11]

The surface morphology, size distribution and elemental composition of $NaCrP_2O_7$ were characterized using a Scanning Electron Microscope (SEM) coupled with Energy Dispersive X-ray Spectroscopy (EDX). To identify the size and shape of the particles and to perform a morphological study of $NaCrP_2O_7$, we use the Scanning Electron Microscope (SEM) observations. Figure 3 illustrates the grain size distribution histogram of $NaCrP_2O_7$ and the inset shows the (SEM) micrograph of the named compound. According to this Figure, the particle size extends from 0.5 to 4 μm on the histogram, with an average size of 1.72 μm indicating the formation of micrometric particles. This small size of the particle indicates the success of micro-particle synthesis [12].

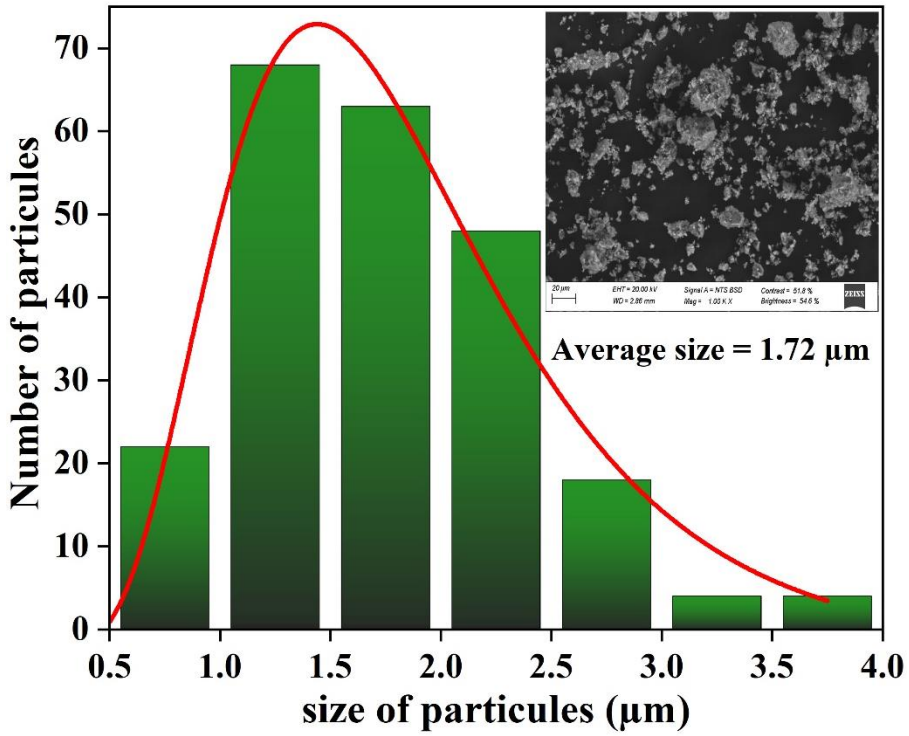

Figure 3. Histogram of grain size distribution of $NaCrP_2O_7$. The inset corresponds to SEM image with an average size around 1.72 µm

Figure 4 shows the EDX spectrum of $NaCrP_2O_7$. This spectrum shows the presence of the peak C which is associated to the emission of the carbon ribbon used during the measurement. We observe that P and O are the main components, while Na and Cr are present in low amounts. Table 1 presents the outcomes of the quantitative EDX spectrum analysis of the elements present in $NaCrP_2O_7$.

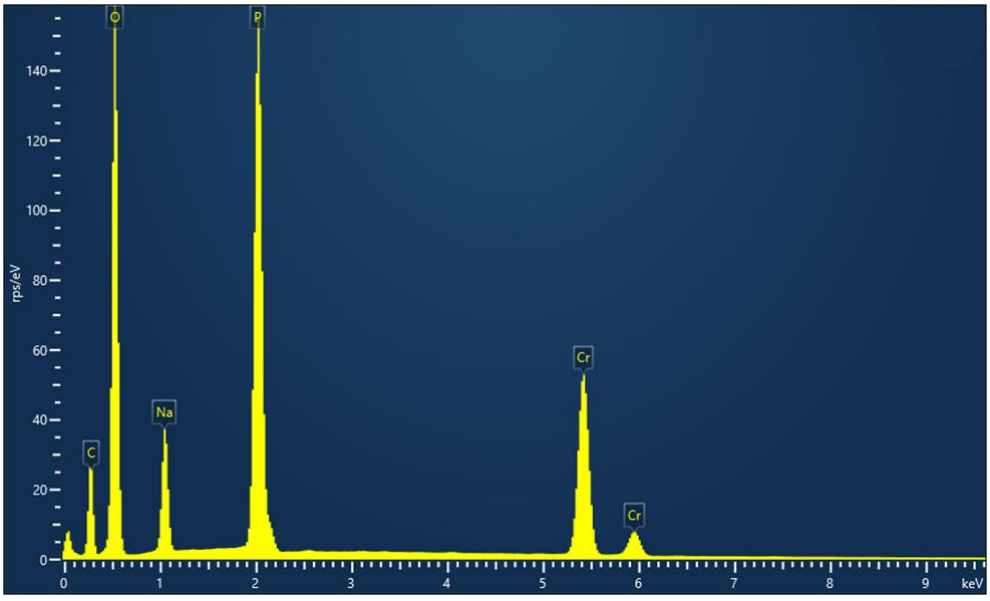

Figure 4. The quantitative analysis of the compositional elements presents in $NaCrP_2O_7$ using EDX

Table 1: The elements present in $NaCrP_2O_7$ and their percentage of occupation.

Spectrum label	EDX Spectrum (%)
C	9.75
Na	11.08
P	51.35
Cr	27.82
Total	100.00

3.2. Determination of the optical band gap (E_g) and the Urbach (E_u) energies

The determination of E_g band gap is obtained firstly through the Marotti method. Figure 5 represents their reflectance curve versus λ. The value of E_g is determined from the maximum of the curve dR/dλ [13]. We found a band-gap energy at 3.15 eV (see the inset of Figure 5).

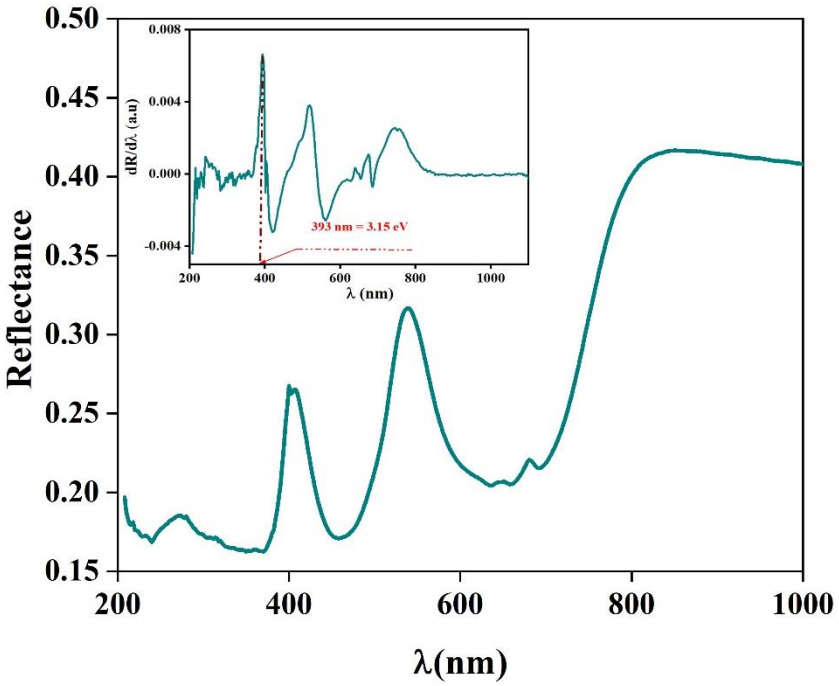

Figure 5. Curve of the reflectance versus λ. The inset of this figure illustrates the evolution of the dR/dλ versus λ.

In the following, the value of E_g for $NaCrP_2O_7$ is found by the use of the Tauc method based on the well-known quadratic equation [14]:

$$\boldsymbol{\alpha h\nu = A(h\nu - E_g)^n} \quad \textbf{(1)}$$

Where h is the Planck constant, ν is the photon's frequency, E_g is the band gap energy and A is a constant. In this equation, the exponent value n depends on the nature of the band gap which is 1/2 for an allowed direct band gap and has the value 2 for an allowed indirect bandgap [15]. Figure 6 shows the plot of $(\alpha h\nu)^2$ and $(\alpha h\nu)^{1/2}$ against photon energy (hν). From this plot, we found the optical energy band gap for direct transition E_{gd} at 2.9 eV and indirect transition E_{gi} at 2.3 eV.

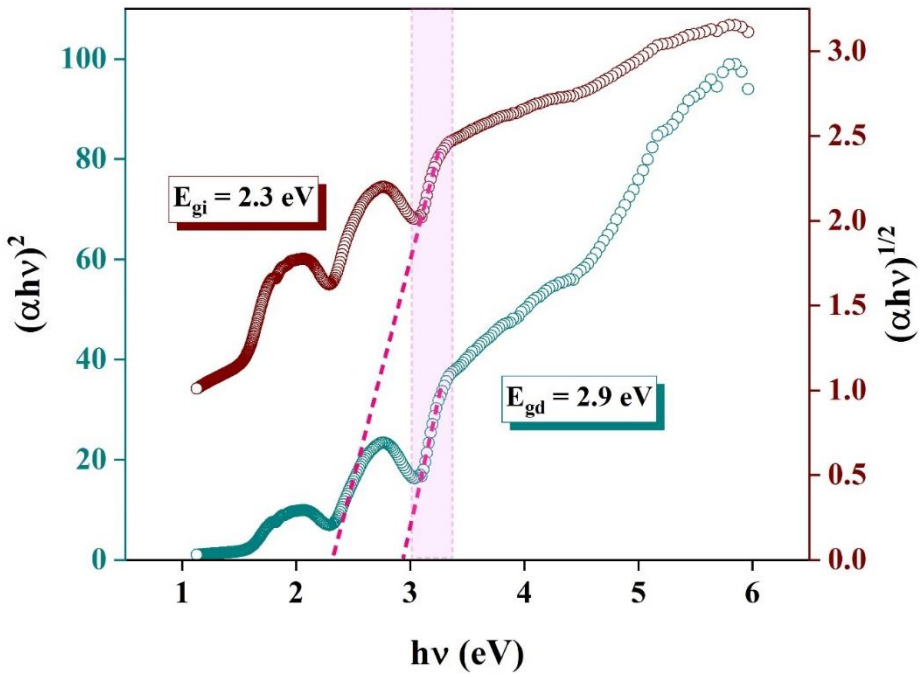

Figure 6. The evolution of $(\alpha h\nu)^{1/2}$and $(\alpha h\nu)^2$against (hν).

To confirm the nature of the optical band gap (direct or indirect), we rearrange Equation (1) and we obtain the following relation:

$$\boldsymbol{Ln(\alpha h\nu) = LnA + n\, Ln(h\nu - E_g)} \qquad \textbf{(2)}$$

Figure 7 shows the evolution of Ln(αhν) against Ln(hν-2.9) for $NaCrP_2O_7$. This curve demonstrates a straight line whose slope gives the power factor (n = 0.48), which is close to 0.5. This value indicates that our sample belongs to the wide optical band gap semiconductor range and has a direct band gap transition. This obtained value is close to the value obtained by Marotti method.

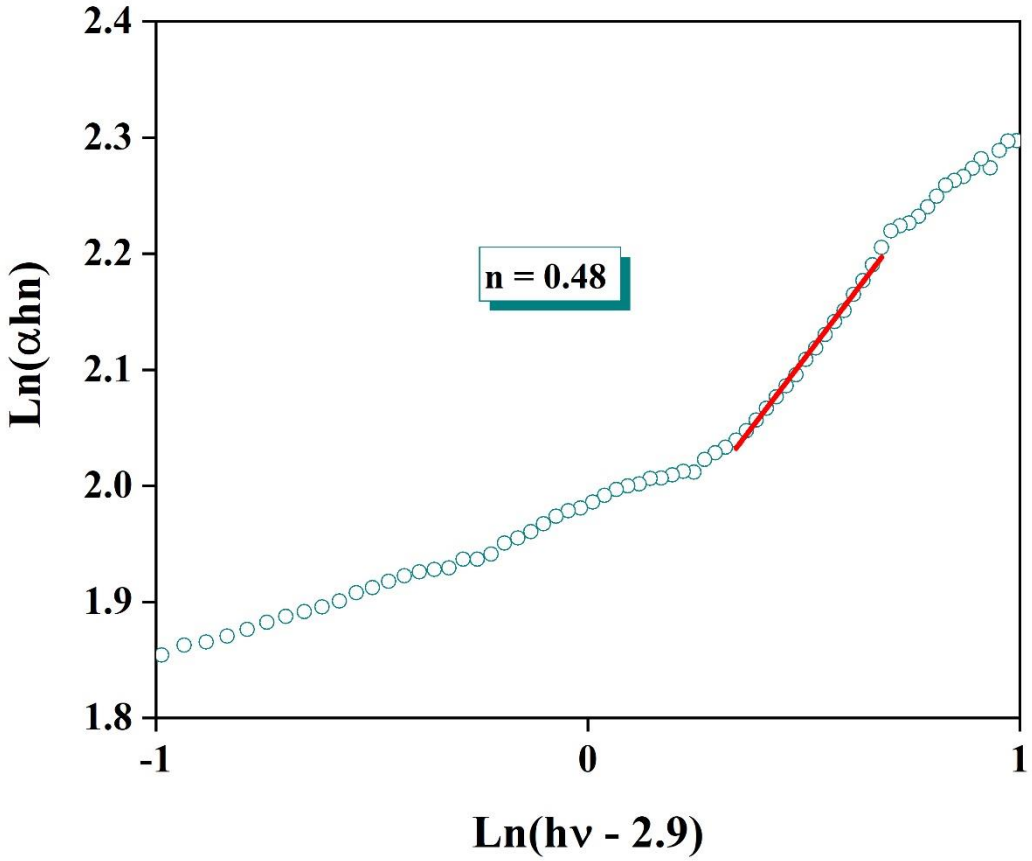

Figure 7. Evolution of Ln(αhν) against Ln(hν-2.9) for $NaCrP_2O_7$.

When impurities are present in semiconductors, phonon interaction often leads to the formation of a band tailing within the band gap. The Urbach energy is a parameter that characterizes the disorder in a sample. It represents the transitions between localized states of the conduction band and extended states of the valence band. The disorder named E_u is calculated by using the following relation where B designates a constant (the band tailing parameter) [16]:

$$\alpha(h\nu) = B\ exp(\frac{h\nu - Eg}{E_u}) \quad (3)$$

By plotting the Ln(α) curve versus hν photon energy, one can determine the Urbach energy. As shown in Figure 8, we calculate it by taking the reciprocal of the slope of the linear portion of the curve. The Urbach energy defines the amount of disorder in the semiconductor. We find E_u= 0.44eV. This value represents 15.17 % of the band gap energy and confirms the presence of the localized states' density in this compound.

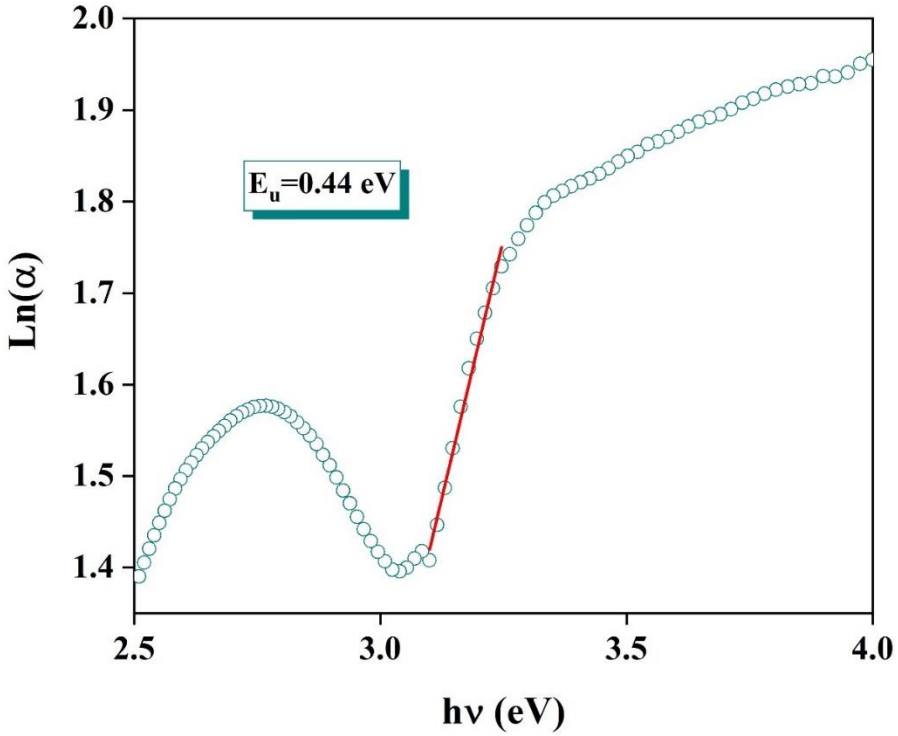

Figure 8. Curve of Ln(α) against hν to determine the Urbach energy for the $NaCrP_2O_7$ compound.

4. Study of the absorption spectrum of Cr^{3+} in $NaCrP_2O_7$ phosphate containing interference dip

First series transition metal ions with the electronic configuration $3d^n$ are sensitive to their surroundings. The strong interaction is thus evident in the $3d^3$ electrons, which are strongly influenced by the vibrations found in the host matrix.

This behavior manifests itself in the optical spectrum through the broad optical absorption bands. Figure 9 illustrates the optical absorption spectrum of Cr^{3+} in $NaCrP_2O_7$ recorded at ambient temperature. The spectrum indicates two broad bands attributed to the spin allowed transitions from ground state $^4A_{2g}(^4F)$ to the excited states $^4T_{2g}(^4F)$ and $^4T_{1g}(^4F)$. In addition to that, we remark the presence of an interference dip on the broad band $^4T_{2g}(^4F)$ and caused by the superposition of the spin forbidden transitions $^4A_{2g}(^4F) \rightarrow {}^2Eg(^2G)$. The examination of this spectrum has a lengthy and disputed historical analysis [17-19].

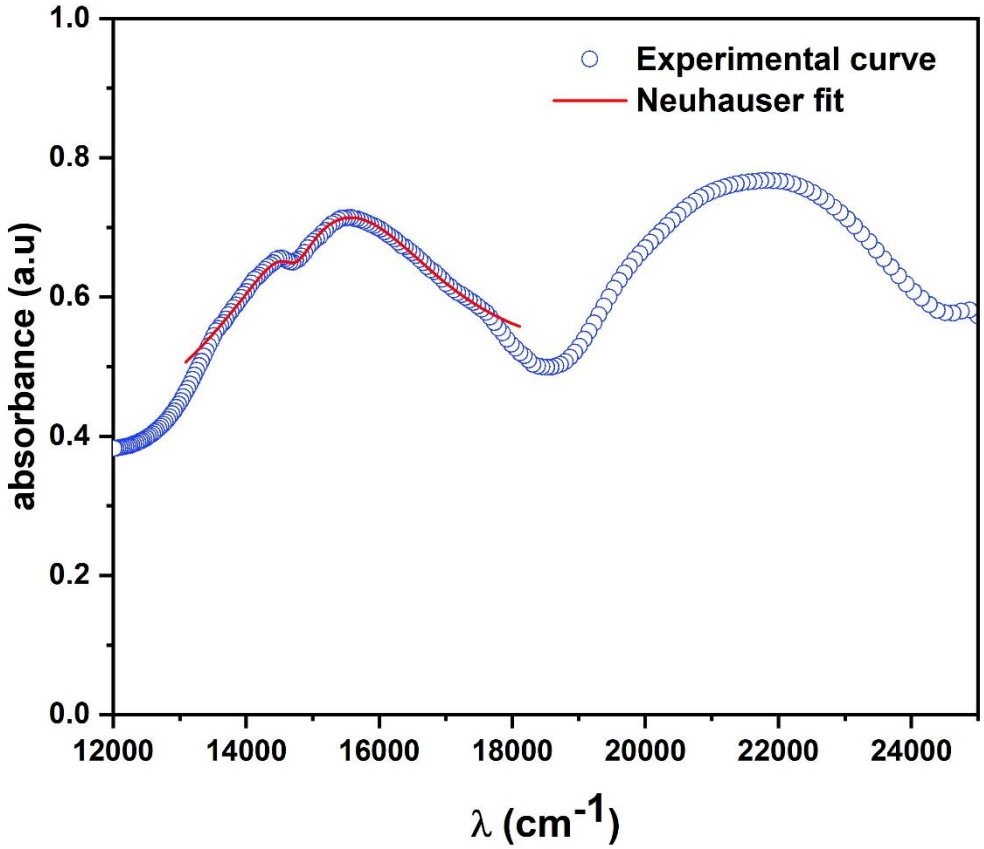

Figure 9. Absorption spectrum of $NaCrP_2O_7$ phosphate and result of the interference dips fitting.

The origin of the interference dip is the interaction between states with different multiplicities of spins. The usual diabatic Hamiltonians are used to describe the total electron-nuclear Hamiltonian for the coupled state [20]:

$$H = \frac{p^2}{2m} + \begin{bmatrix} \frac{1}{2} m\omega_F^2 x^2 + \varepsilon_F & \gamma \\ \gamma & \frac{1}{2} m\omega_A^2 (x - x_A)^2 + \varepsilon_A \end{bmatrix} \quad (4)$$

where m is the mass of the oscillator, ω_A and ω_F are the allowed and forbidden state frequencies, x is the vibrational coordinate, x_A is the shift of the vibrational coordinate minimum upon excitation, ε_A and ε_F are the allowed and forbidden state minimum potential energy, and γ is the coupling constant between the two states. The system under examination is depicted in Figure 10, together with the potential energy surfaces for the ground and excited states that result in the dips.

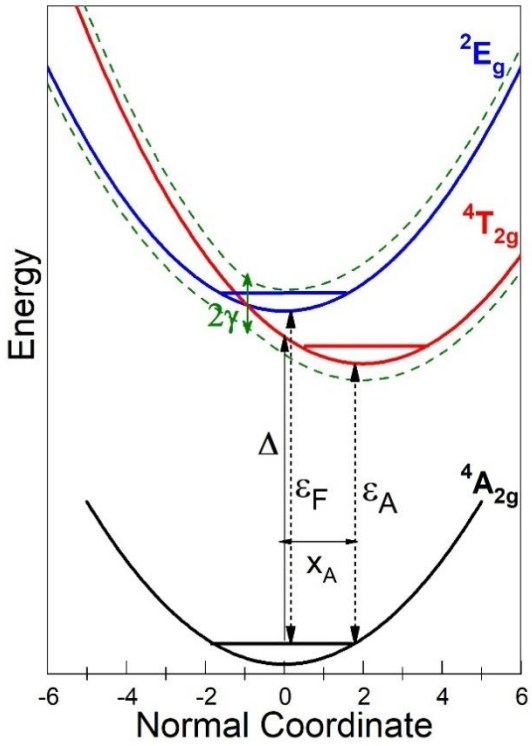

Figure 10. The potential energy surfaces that represent the diabatic (bold lines) and adiabatic (dashed lines) model for $(CrO_6)^{3-}$, as described by Equation (4). The allowed state ($^4T_{2g}$) is labelled "A" and the forbidden state (^2E_g) is labelled "F". The transitions from the ground state $^4A_{2g}$ to the excited states $^4T_{2g}$ and ^2E_g are shown by the arrows.

In the following, we will be employing the Neuhauser method which serves two primary purposes: on the one hand to have a precise reading of the $^4T_{2g}(^4F)$ and $^2E_g(^2G)$ levels and on the other hand to have parameters for tracing the potential energy surfaces which explains the origin of this dip. A concise recapitulation of the method proposed by Neuhauser et al. [20] and Bussièreet al. [21] is provided. In general, the following analytical expression describes the profile of the absorption spectrum with one or two interference dips (m = 1 or 2):

$$\sigma(\omega) = -\frac{1}{\pi} Im\left[\frac{\beta}{1-(\gamma_1^2\alpha_1+\gamma_2^2\alpha_2)\beta}\right] \quad (5)$$

Where γ_1 and γ_2 are the coupling constants of both forbidden state α_1 and α_2 with the allowed one. ω is the frequency, β is the spectrum without coupling, The α and β equations are:

$$\beta = \frac{1}{\omega-\Delta+i\sqrt{\omega_0\lambda_e}} \quad (6)$$

$$\alpha_m = \frac{1}{\omega-\varepsilon_{F,m}+i\Gamma_m} \quad m = 1, or\ 2 \quad (7)$$

The width of individual vibronic lines is determined by Γ_m, a phenomenological damping factor, where Δ is the maximum of the absorption band without coupling and $\varepsilon_{F,m}$ are the energies of each forbidden state. The width of the allowed band is denoted by $\sqrt{\omega_0\lambda_e}$, where $\lambda_e = \Delta - \varepsilon_A$ and ω_0 is the metal-ligand band's stretching frequency.

The absorption spectrum is fitted by:

$$Re[\sigma(\omega)] = -\frac{A}{\pi}\frac{\frac{-\sqrt{\omega_0\lambda_e}-\sum_i\frac{\Gamma_i\gamma_i^2}{\left(\omega-\varepsilon_{F,i}\right)^2+\Gamma_i^2}}{(\omega-\Delta)^2+\omega_0\lambda}}{[1-\sum_i\frac{\gamma_i^2\left((\omega-\Delta)\left(\omega-\varepsilon_{F,i}\right)-\Gamma_i\sqrt{\omega_0\lambda_e}\right)}{\left(\left(\omega-\varepsilon_{F,i}\right)^2+\Gamma_i^2\right)\left((\omega-\Delta)^2+\omega_0\lambda_e\right)}]^2+[\sum_i\frac{\gamma_i^2\left(\left(\omega-\varepsilon_{F,i}\right)\sqrt{\omega_0\lambda_e}+(\omega-\Delta)\Gamma_i\right)}{\left(\left(\omega-\varepsilon_{F,i}\right)^2+\Gamma_i^2\right)\left((\omega-\Delta)^2+\omega_0\lambda_e\right)}]^2} \quad (8)$$

Equation (8) was programmed in the Origin software and the parameters were optimized to obtain the best possible agreement with the experimental spectrum. We applied the Equation (8) only for one interference dip as it is observed on the $^4T_{2g}(^4F)$ band of Figure 9. The energies of $^4T_{2g}(^4F)$ and $^2E_g(^2G)$ are crucial to identify the position of the dip. After the software calculates these energies, the coupling and damping become essential variables in the fitting process. The best fitting, is obtained by the interplay between γ and Γ parameters. The optimal fit's parameter values are presented in Table 2. It is clear that the calculation duplicates very well with the absorption spectrum and the dip is effectively replicated by the use of the analytical equation (Equation (8)). It's crucial to emphasize that the energy of the doublet state ($\varepsilon_F = {}^2Eg(^2G)$), is found in the depth of dip and not at the maximum of the peak. The value of the parameter Δ=E($^4T_{2g}(^4F)$) represents the energy at the maximum of broad band which is approximately at its center. The Γ parameter translates the depth of the dips. The coupling constant between $^2E(^2G)$ and $^4T_2(^4F)$ has a value of γ = 275 cm^{-1}. The γ parameter is related to the S-O coupling constant by $\gamma = -\xi\sqrt{6}/\sqrt{5}$ [19] thus giving ξ = 251 cm^{-1}.

Table 2: Fitting parameters in cm^{-1} with Equation (8) for the calculation of the absorption spectra of Cr^{3+} in $NaCrP_2O_7$.

band	$^4A_{2g} \rightarrow {}^4T_{2g}(^4F)$
Δ	15342
$\sqrt{\omega_0\lambda_e}^*$	2050
λ_e	6618
$\varepsilon_F(^2E_g(^2G))$	14710
Γ	260
γ	275

$^{*}\omega_o$ = 635 cm^{-1} (totally symmetric Cr-O stretching mode of CrO_6^{3-}) [22,23]

4.1. Identification of the absorption spectrum by Crystal field study of the Cr^{3+} in $NaCrP_2O_7$

Crystal Field Theory (CFT) describes the electronic structure and properties of transition metal complexes. This theory is particularly applicable to coordination compounds, where a central metal ion is surrounded by a set of ligands (atoms or molecules that coordinate to the metal) and the interaction between them is treated as purely electrostatic. The ligands, which are typically negatively charged, create a crystal field around the metal ion by influencing the distribution of its d-electrons. The interaction with ligands causes the degenerate d orbitals of the metal ion to split in energy. Crystal Field Theory is a useful tool for predicting and explaining the observed colours, magnetic properties, and electronic spectra of transition metal complexes [24-25].

The energy levels of Cr^{3+} ions in $NaCrP_2O_7$ phosphate are calculated using the following total Hamiltonian [26-30]:

$$\mathbf{H = H_0 + H_{ee}(B,C) + H_{Trees}(\alpha) + H_{CF}(Dq) + H_{SO}(\zeta)} \quad \mathbf{(9)}$$

In Equation (9), the total Hamiltonian H involves the Hamiltonian configuration H_0, the electron-electron repulsion term H_{ee}, which is expressed as a function of the Racah parameters B and C [31-33]. The resulting Hamiltonian H_{ee}, for Cr^{3+} in a $3d^3$ configuration, provides the ^{2S+1}L terms, known as the Russell-Saunders terms, including two quartet terms (^4F and ^4P) and six doublet terms (^2H, ^2G, ^2F, and ^2P). The H_{Trees} Hamiltonian includes the Trees correctionand is dependent on the structure fine $\boldsymbol{\alpha_{Tree}}$ parameter [34,35]. In the case of octahedral symmetry (O_h), the crystal field Hamiltonian (H_{CF}) is given by [36,37]:

$$\mathbf{H_{CF}} = \mathbf{21}\boldsymbol{Dq}\left[\mathbf{C_0^{(4)}} + \sqrt{\frac{5}{14}}\left(\mathbf{C_0^{(4)}} + \mathbf{C_{-4}^{(4)}}\right)\right] \quad \mathbf{(10)}$$

The parameter Dq signifies the ligand field splitting in the crystal field Hamiltonian H_{CF} and it is commonly used in describing the structure of transition metal ions. The Racah tensor algebraic methods, as referenced in [38], are employed for numerical calculations of the matrix elements of C_q^k operators. In the crystal field theory, the splitting of the d orbitals in a transition metal complex gives rise to characteristic absorption bands in the optical spectrum. By examining these spectra, the values of parameters B, C, and Dq can be deduced. These parameters are crucial for understanding the electronic properties of the system. The spin–orbit coupling Hamiltonian H_{SO} depends on ζ parameter which represents the strength of the interaction between the electron's spin and its orbital motion within an atom. The α_{Tree} and ζ parameters are calculated from the equations [28-29]:

$$\boldsymbol{\alpha_{Trees} = N^4\alpha_0 \text{ and } \zeta = N^2\zeta_0} \quad \mathbf{(11)}$$

where the parameter N describes the average reduction factor due to covalency [28] is defined as follows:

$$\mathbf{N^2} = \frac{1}{2}\left(\sqrt{\frac{B}{B_0}} + \sqrt{\frac{C}{C_0}}\right) \quad \textbf{(12)}$$

The free ion Cr^{3+} parameters B_0, C_0, α_0 and $\zeta_0$are illustrated in Table 3 [31-33].

Figure 11. illustrates the Stark levels obtained by splitting of the energy levels of free Cr^{3+}ions with a $3d^3$ configuration in a crystal field with octahedral O_h site symmetry.

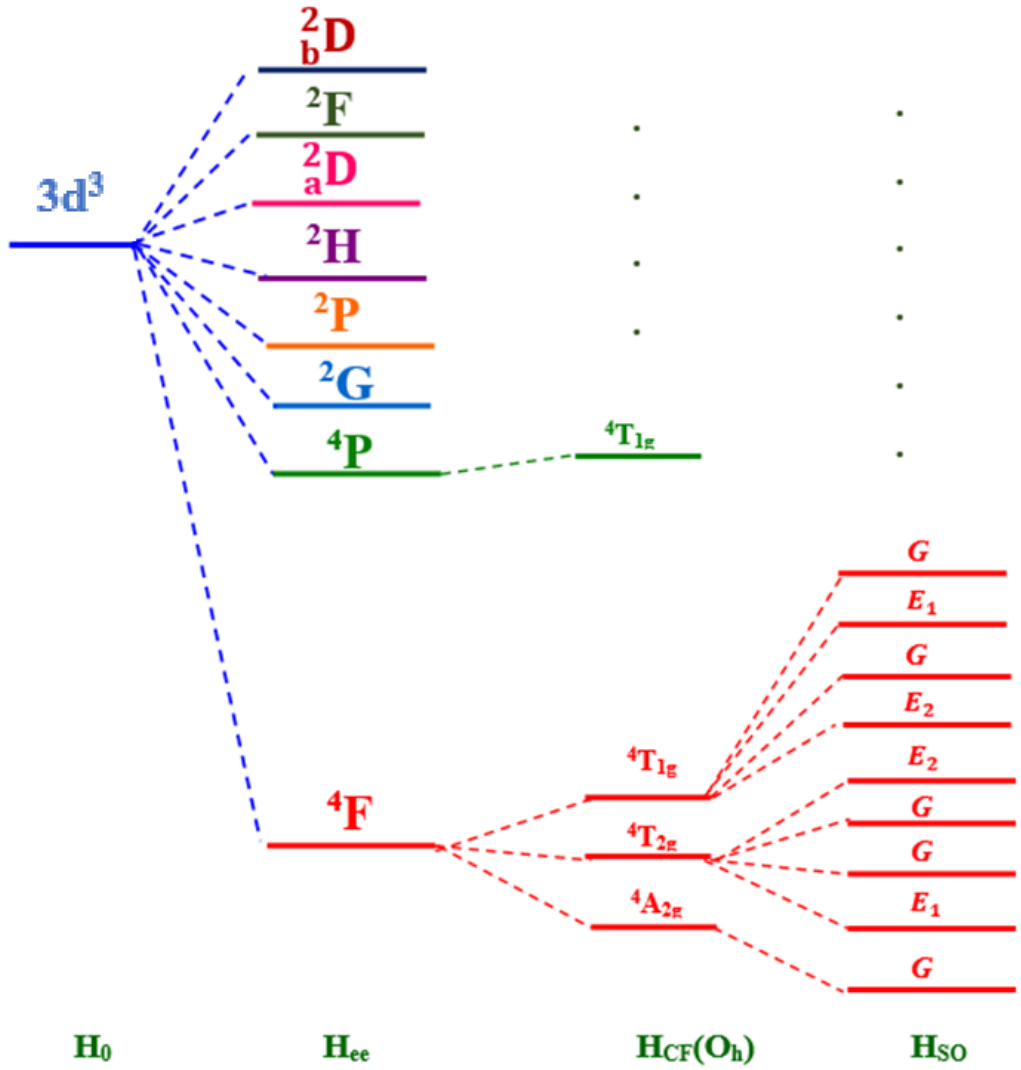

Figure 11. Energy levels of the $Cr^{3+}(3d^3)$ ion under the effect of a crystal field of O_h symmetry and spin-orbit coupling.

The theoretical calculation of the energies for Cr^{3+} ions in $NaCrP_2O_7$ phosphate are obtained by diagonalizing the Hamiltonian of Equation (9). It consists of a 120x120 matrix in the free ion eigenstates $\{|L\ S\ M_L M_S\rangle\}$ within the quartet terms (^4F ground state and ^4P excited state) and doublet

excited terms (^2H, ^2G, ^2F, ^2_aD, ^2_bD and ^2P). For diagonalization, we use a specialized code developed in our laboratorybased on maple software. The computed energies agree very well with Yeung et al.'s results [39], validating and ensuring consistency with our computational approach. The calculated energies obtained after diagonalization are in the form of analytical equations and are expressed in function of the B, C, Dq , αand ζ parameters. The crystal-field parameter Dq is determined based on the absorption energy of the quartet excited state $^4T_{2g}(^4F)$. The Racah parameters B and C are calculated based on the observed quartet $^4T_{1g}(^4F)$ and doublet $^2E_g(^2G)$ excited states, respectively. The values of parameters αand ζ are calculated from Equation (11) and (12). By inputting the relevant parametersB, C, Dq , αand ζ into our package computer, we simulate the electronic structure and energy levels of Cr^{3+} ions in $NaCrP_2O_7$ phosphate. The calculated parameters, listed in Table 3, allow us to deduce the theoretical energy levels of $Cr^{3+}(3d^3)$ in O_h site symmetry (Table 4). Our computational approach, implemented in the developed software package, yields excellent agreement between the calculated stark energy levels and their experimental counterparts.

The Racah parameters B and C experience a reduction relative to their values for free ions, a consequence of covalency effects. With increasing covalency in the host matrix, electrons are distributed somewhat over the ligands, resulting in a decrease in electron-electron repulsion, a phenomenon referred to as the nephelauxetic effect. Table 3 illustrates the values of the ratio $\beta_B = B/B_0$ and $\beta_C = C/C_0$, offering a quantitative measure of the extent of reduction for both parameters.

Table 3: Crystal field, Racah, trees, spin-orbit coupling and nephelauxetic effect parameters values for Cr^{3+} in $NaCrP_2O_7$.

Dq (cm^{-1})	**1534**
B (cm^{-1})	**648**
C (cm^{-1})	**3311**
α (cm^{-1})	**22.58**
ζ (cm^{-1})	**237.37**
Dq/B	**2.36**
C/B	**5.1**
β_B	**0.705**
β_C	**0.801**
B_0 (cm^{-1})[26-27]	**918**
C_0(cm^{-1})[26-27]	**4133**
α_0[26-27]	**30**
ζ_0[26-27]	**275**

Table 4: Experimental and calculated energies (cm^{-1}) of Cr^{3+} in $NaCrP_2O_7$.

O_h	E_{obs}	E_{cal}* *[this work]*	E^a_{cal}* *[this work]*
$^4A_{2g}(^4F)$	0	0	0
$^2E_g(^2G)$	**14710**	14709	14742(4)
$^2T_{1g}(^2G)$		15268	15245(2)
			15267.12(4)
$^4T_{2g}(^4F)$	**15342**	15340	15267.97(2)
			15380(4)
			15582(4)
			15614(2)
$^4T_{1g}(^4F)$	**21729**	21728	21470(2)
			21521(4)
			218657(4)
			21677(2)
$^2T_{2g}(^2G)$	-	21839	22010(4)
			22178(2)
$^2A_{1g}(^2G)$	-	27865	28058(2)
$^2T_{1g}(^2P)$	-	29906	30125(2)
			30175(4)
$^2T_{1g}(^2H)$	-	30303	30391(2)
			30572(4)
$^2E_g(^2H)$	-	32037	32159(4)
$^4T_{1g}(^4P)$	-	34011	33878(4)
			33884(4)
			34910(2)
			33941(2)
$^2T_{1g}(^2H)$	-	34786	34878(2)
			34968(4)
$^2T_{2g}(^2H)$	-	39475	39388(2)
			39463(4)
$^2A_{2g}(^2F)$	-	40824	40836(2)
$^2T_{2g}(^2_aD)$	-	45268	45545(2)
			45656(4)
$^2T_{2g}(^2F)$	-	46989	47012(2)
			47147(4)
$^2E_g(^2_aD)$	-	48958	48996(4)
$^2T_{1g}(^2F)$	-	51664	51617(2)
			51739(4)
$^2T_{2g}(^2_bD)$	-	66633	66494(4)
			66683(2)
$^2E_g(^2_bD)$	-	68314	68337(4)

For Cr^{3+}, the value of k is 0.21 [40], the nature of the bonding is evaluated by the following expression [41]:

$$\boldsymbol{h = \left[\frac{B_0 - B}{B_0 k}\right]} \quad \textbf{(13)}$$

The greater value of h = 1.4 suggests that there is more d-electron delocalization, which suggests that ionic bonding is the main type of interaction between Cr^{3+} and its ligands. The current study indicates that there is a covalent interaction between Cr^{3+} and the ligands since the value of h is less than 1. From the Racah parameters B and C of Table 3 (C/B=5.2), we draw the Tanabe-Sugano diagram for Cr^{3+} ion in an octahedral site symmetry (Figure 12). It displays the overall behavior of Cr^{3+} ion energy levels in terms of Dq/B as a function of local field strength. The case for Cr^{3+} in $NaCrP_2O_7$ phosphate is shown by the vertical line that corresponds to the Dq/B value found by our theoretical computation.

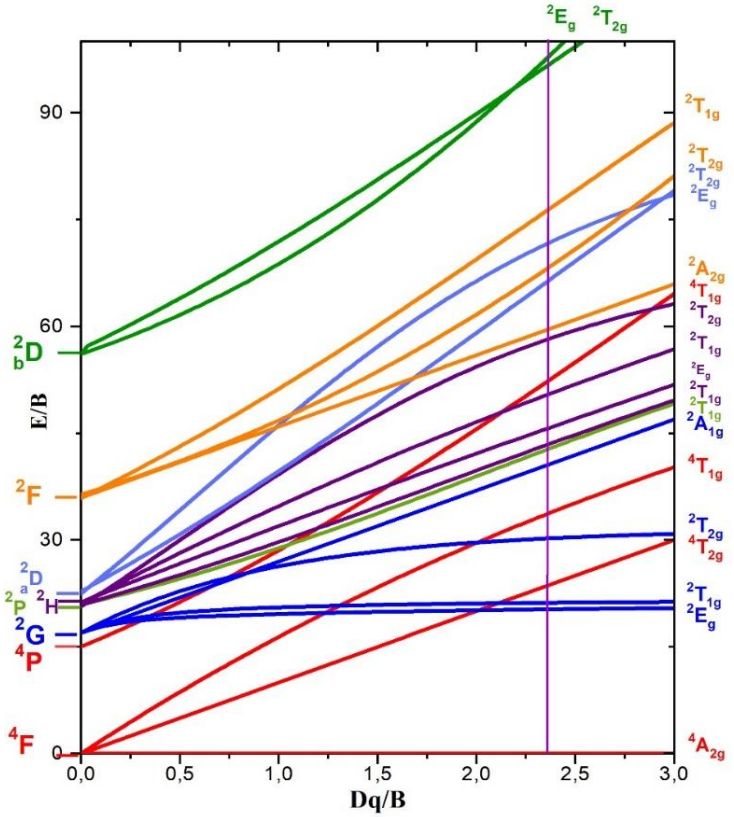

Figure 12. Tanabe Sugano diagram for Cr^{3+} ion in $NaCrP_2O_7$ with C/B=5.2. The vertical line for Dq/B=2.36 represents the case of Cr^{3+}.

We note from this figure that for the computed parameters Dq, B, and C, the electronic states of different multiplicities of spins ^2E_g (^2G) and $^4T_{2g}$ (^4F) close in energy can couple and exchange part of their own character. By spin orbit coupling, the ^2E_g(^2G) and $^4T_{2g}$(^4F) excited states are separated into E_1, E_2, and G states (Figure 13). The mixture of the character between the ^2E_g(^2G) and $^4T_{2g}$(^4F) excited states can only be achieved when the symmetry of the two states under spin orbit coupling is identical (symmetry G). The forbidden transition $^4A_{2g}$(^4F)→ ^2E_g(^2G)acquires some of the permitted character of the spin-allowed transition$^4A_{2g}$(^4F)→ $^2T_{2g}$(^4F)and gains in intensity which is lower compared to the allowed transition.

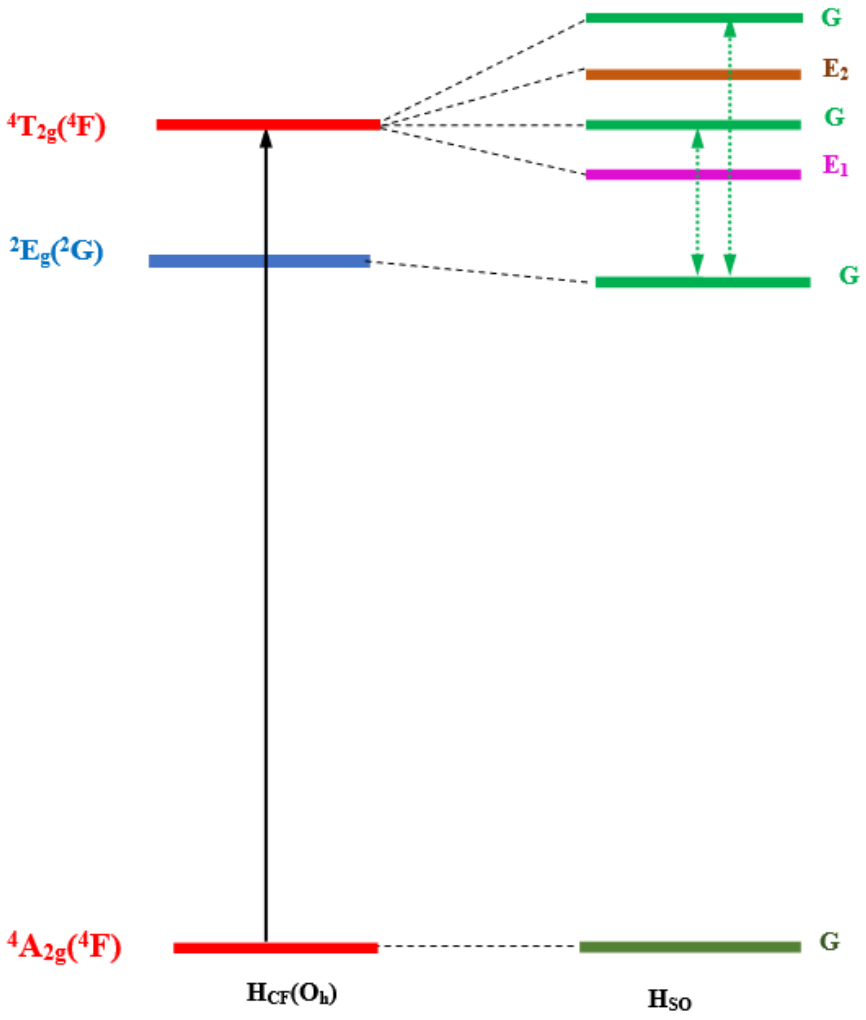

Figure 13. Splitting of Stark levels $^4T_{2g}$ (^4F) and ^2E_g (^2G) under spin-orbit coupling of Cr^{3+} in $NaCrP_2O_7$ phosphate. Spin-allowed transition is indicated by solid arrows. Under spin-orbit coupling, pairs of interacting levels are connected by dot-point arrows.

4.2.The interpretation of the forbidden transition of Cr^{3+} in $NaCrP_2O_7$ with an octahedral site symmetry

In complexes with an inversion symmetry centre, one very efficient way to increase electron-dipole intensity during d-d transitions is via vibronic origin. Odd-parity vibrational modes are always linked to vibronic origins. The selection rules for the O_h point group are shown in Table 5. This Table indicates that the intensity of the spectra in Figure 9 by vibronic mechanisms that involve enabling modes of ungraded parity (a_{1u}, a_{2u}, t_{1u}, t_{2u}, and e_u).

Concerning the octahedron CrO_6 octahedron, by eliminating the translation and rotation modes we have 15 internal vibration modes [8]:

$$\Gamma_{vib} = a_{1g} + e_g + t_{2g} + 2t_{1u} + t_{2u} \quad (14)$$

The t_{1u} mode is active in infrared spectroscopy and the a_{1g}, e_g and t_{2g} active modes are in Raman spectroscopy [8]. The t_{2u} mode is inactive in both spectroscopies [8]. The observation of the d-d transitions can then be explained through vibronic coupling with the infrared active t_{1u} symmetry mode. The observed vibration mode at 635 cm^{-1} on the Raman spectrum of $NaCrP_2O_7$ [22] is assigned to Cr-O symmetric stretching mode (a_{1g}). This assignment is obtained by comparison with the work [23].

Table 5: Selection rules for Cr^{3+} d-d electronic transitions in O_h site symmetry for in$NaCrP_2O_7$ phosphate.

Electronic transition O_h	Electric dipole allowed with Γ_u vibration $\langle\Gamma_i\|T_{1u}\|\Gamma_f\rangle\Gamma_u = A_{1g}$
$^4A_{2g} \rightarrow {}^4T_{2g}$	a_{1u}, t_{1u}, t_{2u}, e_u
$^4A_{2g} \rightarrow {}^4T_{1g}$	a_{2u}, t_{1u}, t_{2u}, e_u

A coupling between two close states with different multiplicities of spins can lead to the emergence of an additional absorption band corresponding to the forbidden transition. These two bands are not the result of a simple sum but are intrinsically linked, giving rise to the appearance of interference that Fano first highlighted in atomic spectroscopy [17-20]. Coupling can occur when

the molecule deviates from the Born-Oppenheimer approximation. In this case, the two potential wells of the excited states are no longer independent of each other. If the nuclei move rapidly, it becomes impossible to transition from one well to the other. In this diabatic approach, the phenomena are described by a potential well scheme similar to what we have seen so far (solid line wells in Figure 10). When the nuclei move slowly, the system can transit from one well to another (considering a non-zero coupling). The crossing between the two wells is no longer 'sealed' as in the diabatic case. The coupling leads to two new wells, or adiabatic wells, whose characteristics are mixed. This approach is represented by the dashed wells in Figure 10. The higher the coupling, the more energetically separated these two wells become.

A single normal coordinate Q is used for the model of coupled potential energy surfaces in order to study the coupling between spin different multiplicity states. Owing to the characteristics of the electronic transition, which correspond to the intra-configuration d-d excitation, the doublet $^2E_g(^2G)$ and the ground $^4A_{2g}(^4F)$ (Q = 0 Å) states share the same vibrational frequency and position of the potential energy minimum [25]. With the amount ΔQ, the $^4T_{2g}(^4F)$ state is shifted to longer metal-ligand bond distances, because the metal-ligand antibonding molecular orbitals are populated by d-d excitation [25]. The magnitude of the displacements ΔQ is determined from the width of the $^4T_{2g}(^4F)$ band of the experimental spectrum. Without spin-orbit coupling, the potentials for the excited states $^2E_g(^2G)$ and $^4T_{2g}(^4F)$ are as follows:

$$V(^2E_g) = V_1 = \frac{1}{2}(kQ^2) + E(^2E_g) \quad (15\text{-a})$$

$$V(^4T_{2g}) = V_3 = \frac{1}{2}(k(Q - \Delta Q_1)^2) + E(^4T_{2g}) \quad (15\text{-b})$$

where $E(^2E_g)$ and $E(^4T_{2g})$ are the energies of the potential minimum for the $^2E_g(^2G)$, and $^4T_{2g}(^4F)$ states, respectively, and k is the frequency observed on the Raman spectrum of $NaCrP_2O_7$ assigned to Cr-O symmetric stretching mode (a_{1g}).

The quartet $^4T_{2g}(^4F)$ and the doublet ^2E_g excited levels divided into (G, E_1 and E_2) states if we consider the spin-orbit coupling, as Figure 13 shows. The uncoupled (diabatic) potentials, resulting in the absence of spin-orbit coupling are illustrated in Figure 14.a For the sake of simplification, Figure 14.b only displays the derivative states that have G irreducible representations.

The curves obtained from Equation (15) cannot describe the spin forbidden transition $^4A_{2g}(^4F) \rightarrow {}^2E_g(^2G)$ detected in the absorption spectrum (Figure 9). Table 6 lists the spectroscopic

parameters that were employed to compute the G diabatic potential energy curves that emerged from the $^2E_g(^2G)$ and $^4T_{2g}(^4F)$ excited states.

Table 6: The spectroscopic parameters derived from the $^2E_g(^2G)$ and $^4T_{2g}(^4F)$ excited states.

Parameters	$NaCrP_2O_7$
k(cm^{-1})	635
ΔQ ($^4T_{2g}$) (Å)	1.86
λ (cm^{-1})	$\xi/3 = 79.12$
γ(cm^{-1})	$-3\lambda\sqrt{6/5} = -259$
E_{00} G(^{2}Eg)	14742(4)
E_{00} $E_1(^4T_{2g})$	12551(2)
E_{00} G($^4T_{2g}$)	12664(4)
E_{00} $E_2(^4T_{2g})$	12866(4)
E_{00} G($^4T_{2g}$)	12898(2)

Doublet excited state G(^2E_g) can interact with the $^2G(^4T_{2g})$, $E_1(^4T_{2g})$ and $E_2(^4T_{2g})$ states. According to this analysis, the doublet states receive most of their intensities from the allowed quartet transitions and the spin forbidden transition $^4T_{2g}(^4F) \rightarrow {}^2E_g(^2G)$ can arise from the interaction of the $3d^3$ electrons of Cr^{3+} with the $NaCrP_2O_7$ host matrix. The observed spin-forbidden transitions between the $^4A_{2g}(^4F)$ ground state and the $^2E_g(^2G)$, excited state are caused by the interaction between the same symmetry levels (G) derived from electronic states of different multiplicities [8]. Effectively, a constant with a magnitude proportional to the spin-orbit coupling $\lambda(-3\lambda\sqrt{6/5})$ [42] are considered to mix the characters of the $^4T_{2g}(^4F)$, and $^2E_g(^2G)$diabatic potentials. In this situation, the coupled potentials' matrix (adiabatic potentials) 2x2 is expressed in the following:

$$V(^2E_g, {}^4T_{2g}) = \begin{pmatrix} V(^4T_{2g}) & -3\lambda\sqrt{6/5} \\ -3\lambda\sqrt{6/5} & V(^2E_g) \end{pmatrix} \quad (16)$$

The diagonals Terms in Equation (16) represent the equations of the diabatic potential energy wells and are therefore identical to those of Equation (15). The diabatic/adiabatic approach will considerably modify the appearance of the theoretical absorption spectrum and the appearance of observed forbidden transitions experimentally, such as the band corresponding to states $^4T_{1g}(^4F)$ and

^2E_g of the Figure 9, will appear in the calculation. The adiabatic potentials state surfaces, obtained from Equation (16) and from the spectroscopic parameters shown in Table 6, are depicted in Figure 14.c. The spin-forbidden $^4A_{2g}(^4F) \rightarrow {}^2E_g(^2G)$ transitions are caused by the adiabatic excited state potential energy curves V_+ and V_-, which are produced when the spin-orbit coupling between $^4T_{2g}(^4F)$ and $^2E_g(^2G)$ is taken into account.

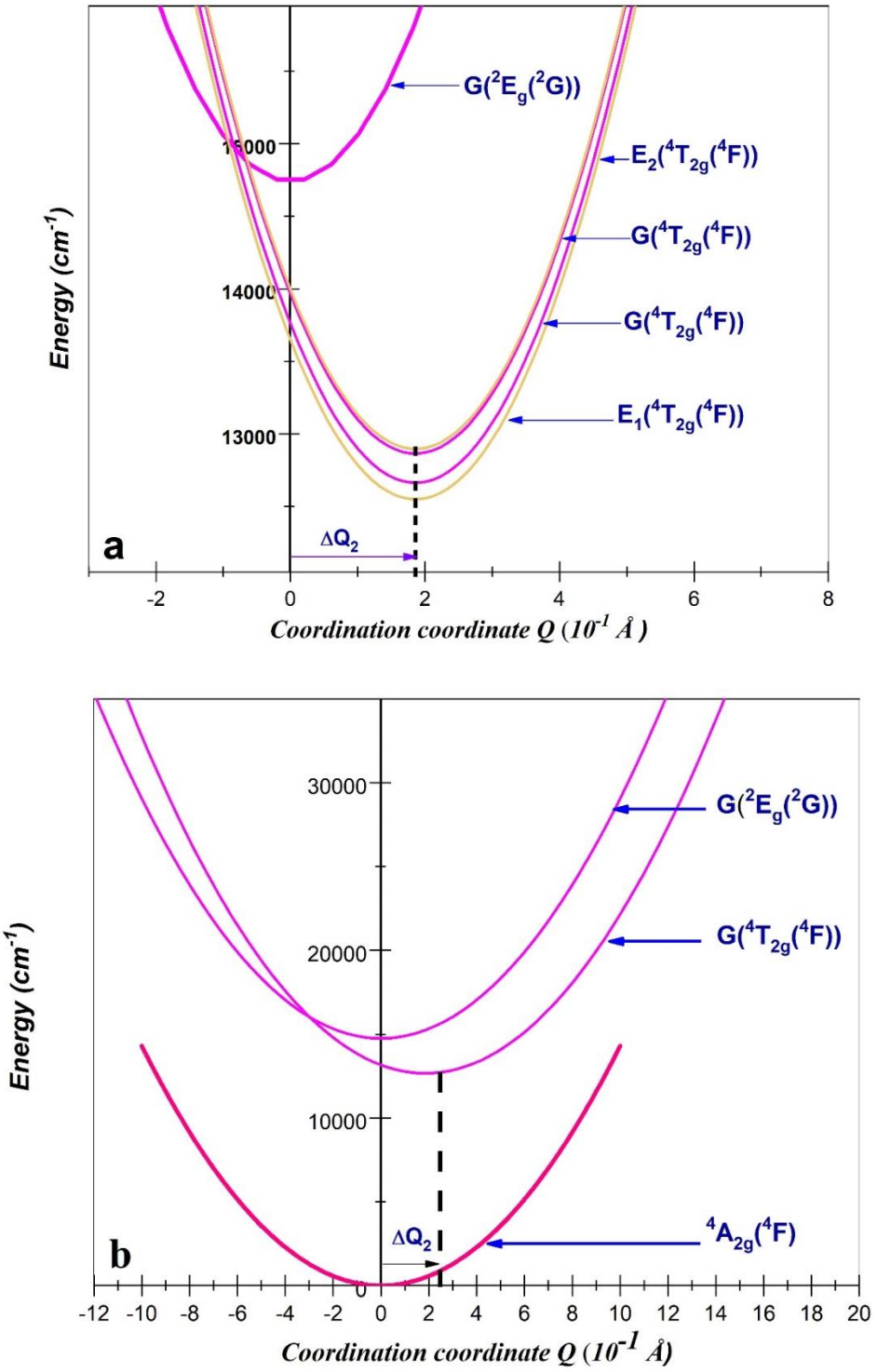

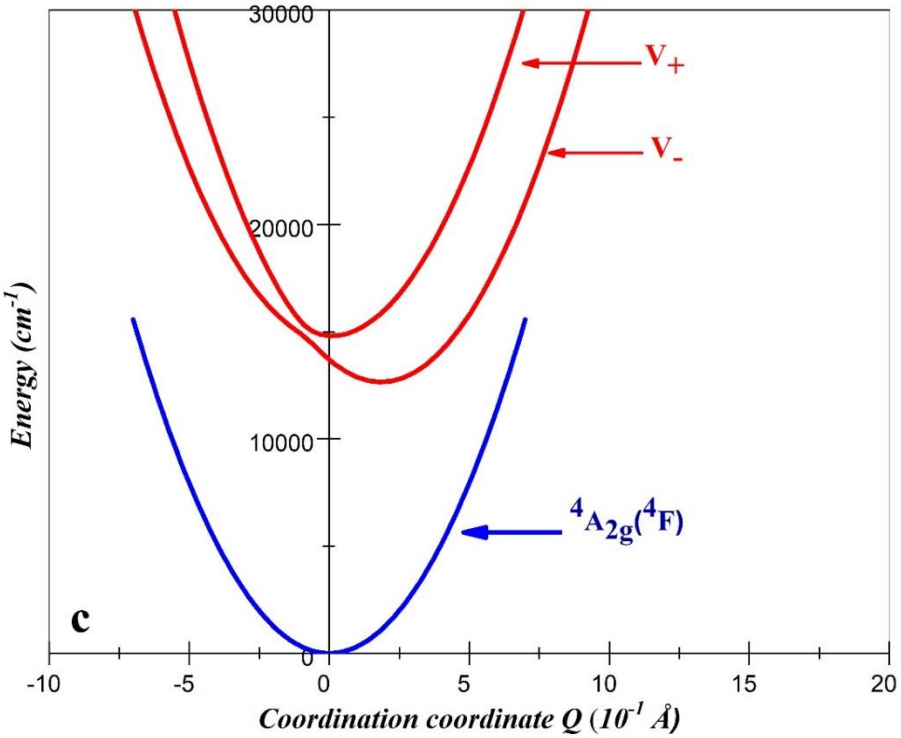

Figure 14. a) Diabatic potential curves for uncoupled states b) We present only the G states emerging from ^2E_g, $^4T_{2g}$for simplicity c) The adiabatic potentials energy curves emerging from the $^2E_g(^2G)$ and $^4T_{2g}(^4F)$ electronic states.

The modelling of absorption spectrum of Figure 9 is carried out using the autocorrelation function $\langle\varphi|\varphi(t)\rangle$. This function depicts the dynamic evolution of the wave function from the initial state within a potential energy well corresponding to the final state. The Fourier transformation of the autocorrelation yields the absorption spectrum, which is the overlap of φ(t) with φ(t=0) [8]:

$$I_{lum}(\omega) = C\omega^3 \int_{-\infty}^{+\infty} e^{i\omega t} \left\{ \langle\langle\varphi|\varphi(t)\rangle\rangle e^{-\Gamma^2 t^2 + i\frac{E_{00}}{\hbar}t} \right\} dt \qquad (17)$$

The evaluation of the autocorrelation function is facilitated by assuming (i) that the potential energy wells are harmonic and the force constants are identical for the initial and final states, (ii) that the transition dipole moment is constant, and (iii) that the normal coordinates of the two states are identical. In this case, the autocorrelation equation takes the following analytical form [8]:

$$\langle\varphi|\varphi(t)\rangle = \exp\left(\sum_j [-\frac{\Delta Q_j^2}{2}(1 - e^{ik_j t}) - \frac{ik_j t}{2}]\right) \qquad (18)$$

Here, the energy of the origin is denoted by the word E_{00}, the absorption spectrum's frequency is ω, and the phenomenological damping factor Γ controls the width of each line in the spectrum. Wavenumber units are used for all amounts. The vibrational frequencies of each mode and the displacement along the normal coordination Q_j of the potential surfaces are denoted by the words kj

and ΔQ_j. Frequency of 635 cm^{-1} is considered for k. The experimental spectrum is fitted by adjusting the parameters E_{00}, Γ, and ΔQ. Table 7 lists the values that were obtained.

Table 7: Parameters used to calculate the Luminescence spectrum shown in Figure 3.

Parameters	values
$E_{00}(^2E(^2G))$ (cm^{-1})	14742
Γ (cm^{-1})	35
k_1(cm^{-1}), ΔQ_1 (dim, less)	635, 0
$E_{00}(^4T_{2g}(^4F))$ (cm^{-1})	12664
Γ (cm^{-1})	20
k_2(cm^{-1}), ΔQ_2 (dim, less)	635, 1.86

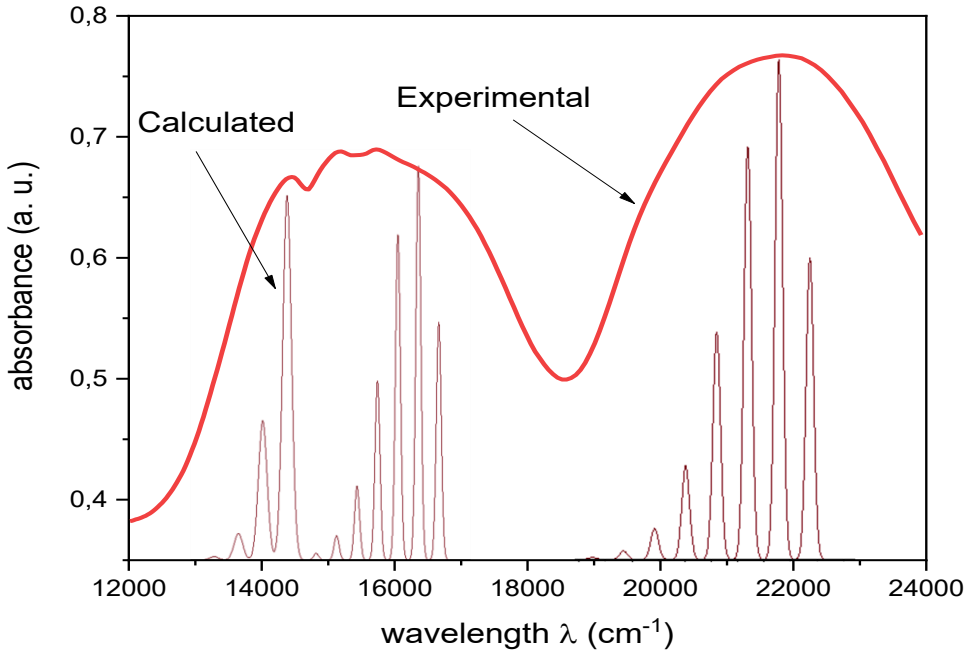

Figure 15. Experimental and calculated absorption spectrum of $NaCrP_2O_7$ phosphate with the interference dips.

The spectroscopic technique known as electron paramagnetic resonance, or EPR, is used to analyze materials that have unpaired electrons. Since chromium ions normally have unpaired electrons and exhibit paramagnetic properties, this characterization technique can detect the presence of traps by measuring the resonance absorption of electromagnetic radiation by the

unpaired electrons in external magnetic fields. Electron Paramagnetic Resonance (EPR) spectroscopy measures the characteristic of EPR signal that is produced when unpaired electrons in chromium ion 3d orbitals absorb electromagnetic radiation in the presence of a magnetic field. Figure 16 depicts the EPR spectrum of the $NaCrP_2O_7$ sample at room temperature. The spectrum shows a resonance signal centred at g = 1.9225. A recent study by Giada Lorenzi et al. [43] on the EPR spectrum of Cr-bearing gahnite ($ZnAl_2O_4$) pigment at X and W band frequencies revealed a resonance signal at g value of 2.05. From comparison with this reference the EPR signal at 1.9225 is due to the Cr^{3+} ions.

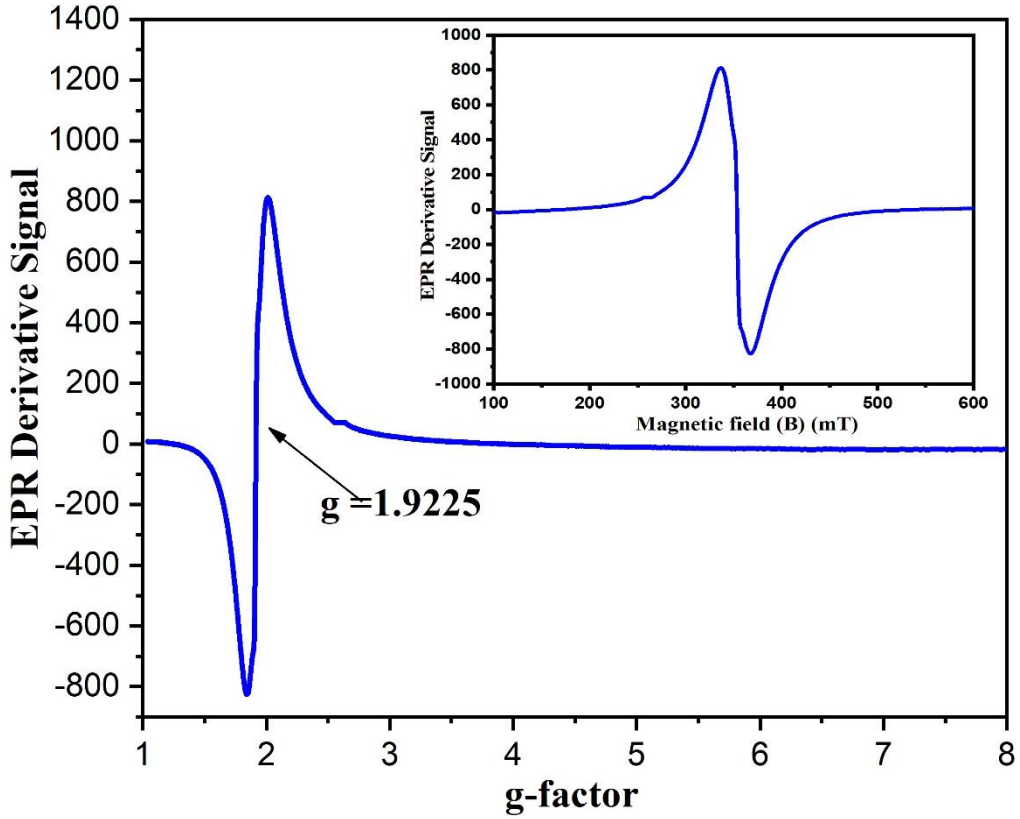

Figure 16. EPR spectrum and g-factor of $NaCrP_2O_7$ at room temperature.

5. Conclusion

This research delved into the synthesis and characterization of $NaCrP_2O_7$ phosphate. The XRD analysis confirmed its monoclinic system with a $P2_1/a$ space group. SEM imaging revealed particle sizes ranging from 0.5 to 4 µm, with an average of 1.72 µm, indicating the formation of micrometric particles. UV/Vis absorption spectra, analysed using Tauc's law and the calculation of Urbach energy, showcased direct transition characteristics, with heightened disorder and defect concentration attributed to the presence of Cr^{3+} ions. Notably, room temperature absorption spectra exhibited an interference dip on the broad band $^4T_{2g}(^4F)$, attributed to the superposition of spin

forbidden transitions $^4A_{2g}(^4F) \rightarrow {}^2E_g(^2G)$, a phenomenon elucidated through the Neuhauser model based on coupled potential energy surfaces. This model yielded insights into the electronic structure of Cr^{3+} ($3d^3$) ions in $NaCr(P_2O_7)$ samples, facilitating the determination of Racah and crystal-field parameters and achieving alignment between theoretical and experimental energy levels. The absorption spectrum was further analyzed using Fourier transformation of the autocorrelation function. Overall, this study contributes to the understanding of $NaCrP_2O_7$ phosphate structures and highlights the potential of synthesized compounds for practical applications in optoelectronic technologies. Additionally, EPR measurements provided valuable insights into various trap types, enriching our comprehension of the electronic structure.

Acknowledgements

I would like to thank the Principal Engineer of the physics department of the Faculty of Sciences of Sfax Mrs DAMMAK Sameh for carrying out the chemical analyzes by UV spectroscopy.

Data availability

No data were used for the research described in this article.

Declaration of competing interest

The authors declare that they have no known competing financial interests or personal relationships that could have appeared to influence the work reported in this paper.

References:

[1] X. Cao, J. Zhou, A. Pan and S. Liang Acta Phys. -Chim. Sin., 2020, 36, 1905018-1905044.

[2] M. Gabelica-Robert, M. Goreaud, Ph. Labbe and B. Raveau, J. Solid State Chem, 1982, 45, 389-395.

[3] M. Sassi, A. Oueslati, N. Moutia, K. Khirouni and M. Gargouri1, Ionics, 2016, 23, 847-855.

[4] R. Masse, J. Bagieu-Beucher, J. Pecault, J. P. Levy and J. Zyss, Nonlinear. Opt., 1993, 5, 413.

[5] A. Zaafouri, M. Megdiche and M. Gargouri, J. Alloys Comp., 2014, 584, 152-158.

[6] M. Krichen, M. Megdiche., K. Guidara and M.Gargouri, Ionics, 2015, 21, 935-948.

[7] R. Pang, C. Li, L. Jiang and Q. Su, J. Alloys Compd., 2009, 471, 364-367.

[8] H. Souissi and S. Kammoun, J. Lumin., 2011, 131, 2515-2520.

[9] O. Taktak, H. Souissi and S. Kammoun, J. Lumin., 2015, 161, 368-373.

[10] A. El Yacoubi, A. Massit, S. El Moutaoikel, A. Rezzouk and B. Chafik El Idrissi, Am. J. Mater. Sci. Eng., 2017, 5, 1-5.

[11] W. C. Hu, C. H. Kao, F. P. Yang, H. C. Jiau and K. F. Ssu; VESTA: 22nd International Conference on Software Engineering and Knowledge Engineering; SEKE Redwood City, CA, United States (2010) 345–348.

[12] Y. Pu, Y. Huang, T. Tsuboi, H. Cheng and H. J. Seo, RSC Adv., 2015, 5, 73467-73473.

[13] R. Mguedla, A. Ben Jazia Kharrat, M. Saadi, K. Khirouni, N. Chniba-Boudjada and W. Boujelben, J. Alloys Compd., 2020, 812, 152130.

[14] J. Tauc and A. Menth, J. Non-Cryst. Solids, 1972, 8-10, 569-585.

[15] Gagandeep, K. Singh, B. S. Lark. and H. S. Sahota, Nucl. Sci. Eng., 2000, 134, 208-217.

[16] S. Kalyanaraman, P. M. Shajinshinu and S.Vijayalakshmi, Physica B, 2016, 482, 38-42.

[17] O. Taktak, H. Souissi and S. Kammoun, Opt. Mater., 2021, 113, 110682.

[18] H. Souissi, O. Taktak and S. Kammoun, Indian J. Phys., 2018, 92, 1153-1160.

[19] O. Maalej, O. Taktak, B. Boulard and S. Kammoun, J. Phys. Chem. B, 2016, 120, 7538-7545.

[20] D. Neuhauser, T. Park and J. I. Zink, Phys. Rev. Lett., 2000, 85, 5304-5307.

[21] G. Bussière, C. Reber, D. Neuhauser, D. A. Walter and J. I. Zink, J. Phys. Chem., 2003,107, 1258-1267.

[22] M. Sassi, A. Oueslati, M. Gargouri, J. Appl. Phys. A., 2015, 119, 763-771.

[23] Gangulibabu, D. Bhuvaneswari and N. Kalaiselvi, Appl. Phys. A, 2009, **96**, 489-493.

[24] P. Rössel, A. Wolfshohl, J. Daniels, and R. Glaum, “Osmium(IV) pyrophosphate: Synthesis, Crystallization, and Ligand-Field Analysis of the [OsIVO6] Chromophore,” ZAAC, vol. 648, no. 10, Mar. 2022.

[25] S. C. Roy, R. Glaum, D. Abdullin, O. Schiemann, N. Quang Bac, and K. Lii, ZAAC, vol. 640, no. 10, pp. 1876–1885, May 2014.

[26] I. Elhamdi, F. Mselmi, S. Kammoun, E. Dhahri, A. Carvalho, P. Tavares, and B. F. O Costa, Dalton Trans., 2023, 52, 9301-9314.

[27] I. Elhamdi, H. Souissi, S. Kammoun, E. Dhahri, A. L. B. Brito, R. Fausto and B. F. O. Costa, J. Lumin., 2023, 263**,** 119968.

[28] O. Taktak, H. Souissi and S. Kammoun, J. Lumin, , 2020, 228, 117563.

[29] H. Souissi, O. Taktak and S. Kammoun, Opt. Mater., 2021, 121, 111529.

[30] O. Taktak, H. Souissi, O. Maalej, B. Boulard and S. Kammoun, Indian J. Lumin., 2016, 180, 183-189.

[31] S. Sugano, Y. Tanabe and H. Kamimura, Multiplets of transition-metal ions in crystals (Academic Press, New York), 1970.

[32] J. S. Griffith, The Theory of transition-metal ions, Cambridge University Press, Cambridge, 1961.

[33] R. C. Powell, Physics of Solid-State Laser Materials, 1th Ed. Springer-Verlag, New York, 1998, pp.215-233.

[34] Z. Y. Yang, C. Rudowicz and Y. Y. Yeung, Physica B, 2004, 348, 151-159.

[35] C. Rudowicz, Z. Y. Yang, Y. Y. Yeung and J. Qin, J. Phys. Chem. Solids., 2003, 64, 1419-1428.

[36] D. J. Newman, B. Ng, Crystal field Handbook, 1th. Cambridge University Press, 2000, pp.28-36.

[37] B. G. Wybourne, Spectroscopic Properties of Rare Earth, 1th Ed. Wiley, New York, 1965, pp.48-234.

[38] J. P. Elliott, B. R. Judd and W. A. Runciman, Proc. R. Soc. London, Ser. A,1957, 240 ,509-523.

[39] Y.Y. Yeung and C. Rudowicz, Comput. Chem., 1992, 16, 207-216.

[40] C. K. Jorgensen and H. Hartmann, Absorption spectra and chemical bonding in complexes, Pergamon Press, Oxford (UK), 1963, pp. 113.

[41] W. Seeber, D. Ehrt and D. Eberdorff-Heidepriem, J. Non-Cryst. Sol., 1994, 171, 94–104.

[42] C. K. Jorgensen and H. Hartmann, Absorption spectra and chemical bonding in complexes, Pergamon Press, Oxford (UK), 1963, pp. 113.
[43] G. Lorenzi, G. Baldi, F. Di Benedetto, V. Faso, L. A. Pardi, and M. Romanelli, J. Eur. Ceram. Soc., 2006, 26, 125-129.